



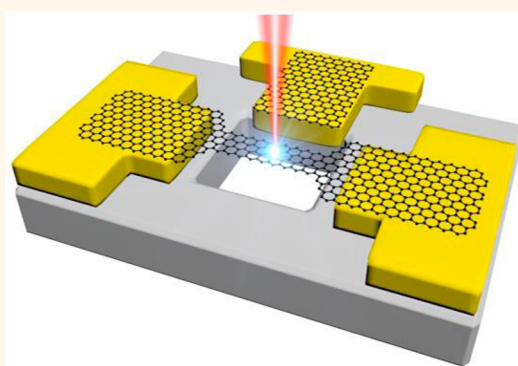
In Situ Transmission Electron Microscopy Modulation of Transport in Graphene Nanoribbons

Julio A. Rodríguez-Manzo,[‡] Zhengqing John Qi,[‡] Alexander Crook, Jae-Hyuk Ahn,[§] A. T. Charlie Johnson,^{*} and Marija Drndić^{*}

Department of Physics and Astronomy, University of Pennsylvania, Philadelphia, Pennsylvania 19104, United States

Supporting Information

ABSTRACT: *In situ* transmission electron microscopy (TEM) electronic transport measurements in nanoscale systems have been previously confined to two-electrode configurations. Here, we use the focused electron beam of a TEM to fabricate a three-electrode geometry from a continuous 2D material where the third electrode operates as side gate in a field-effect transistor configuration. Specifically, we demonstrate TEM nanosculpting of freestanding graphene sheets into graphene nanoribbons (GNRs) with proximal graphene side gates, together with *in situ* TEM transport measurements of the resulting GNRs, whose conductance is modulated by the side-gate potential. The TEM electron beam displaces carbon atoms from the graphene sheet, and its position is controlled with nanometer precision, allowing the fabrication of GNRs of desired width immediately prior to each transport measurement. We also model the corresponding electric field profile in this three-terminal geometry. The implementation of an *in situ* TEM three-terminal platform shown here further extends the use of a TEM for device characterization. This approach can be easily generalized for the investigation of other nanoscale systems (2D materials, nanowires, and single molecules) requiring the correlation of transport and atomic structure.



KEYWORDS: *in situ* TEM, electronic transport, modulation, side gate, graphene nanoribbons, two-dimensional materials

Growing interest in performing *in situ* TEM electronic transport measurements is motivated by the need to understand transport in devices that keep shrinking in size and by a surge of specialized TEM sample holders allowing such measurements. The concept of *in situ* measurements is particularly attractive because standard TEMs offer a unique combination of materials-characterization techniques (high-resolution imaging, electron diffraction, electron-based spectroscopy, *etc.*) that can be used concurrently to correlate a material's structure and chemistry—down to the atomic scale—with its electronic properties. However, *in situ* TEM transport measurements have been confined to two-electrode configurations, by using either two static electrodes or a movable scanning probe tip operating as an electrode. Examples include measurements of chains of Au atoms;^{1–3} C^{4–6} and BN tubes;^{7,8} Si,⁹ Ge₂Sb₂Te₅,¹⁰ and MoSe wires;¹¹ CNT–metal junctions;¹² graphene constrictions^{13–15} and ribbons;^{16–18} atomic C chains;¹⁹ and nanobatteries.^{20,21} Modulating the conductance in some of these nanoscale systems by tuning the charge carrier density requires addition of a third electrode: the gate electrode in a field-effect transistor (FET) configuration.

In this Article, we describe the implementation of a three-terminal transport platform inside the TEM, extending its use beyond two-terminal *in situ* characterizations. Specifically, we present the steps to achieve *in situ* TEM fabrication of a three-electrode graphene device nanosculpted from a continuous graphene sheet, with one graphene electrode operating as a side gate, to perform *in situ* TEM transport measurements in a freestanding graphene nanoribbon (GNR) serving as a FET channel. The top- or bottom-gate configuration typically used to modulate the charge carrier density in a FET channel is incompatible with *in situ* TEM transport studies, where the goal is to image and fabricate the channel with the electron beam. For these types of studies, the side-gate configuration offers a valid alternative by removing the gate from the path of the electron beam, which then can be used to image and modify the channel *via* beam-induced modifications without interruption. In the side-gate configuration the coupling between gate and channel is weaker than in the top/bottom-gate configuration

Received: February 26, 2016

Accepted: March 24, 2016

but, as we show here, sufficiently large to modulate the electronic properties of a GNR FET channel. In summary, this three-terminal device design enables the simultaneous characterization of the channel's structural, chemical, and transport properties within the TEM column (Figure 1a).

In our experiments, the GNRs are suspended between source and drain electrodes and in proximity to the side-gate electrode (Figure 1b). The GNRs and graphene side gates are fabricated with nanometer precision by cutting continuous graphene sheets with a focused electron beam by operating the TEM in scanning mode (STEM).^{22,23} After the *in situ* device fabrication we measure the current I flowing through the GNR for a fixed source–drain voltage V_b while the gate potential V_g is varied. In this way, we modulate the GNR conductance within the TEM column at room temperature (Figure 1c). The sign and magnitude of the measured changes in GNR conductance are explained by considering the electric field strength at the GNR channel, which we estimate with numerical simulations to be a maximum of $\sim 10^7$ V m⁻¹ in our experiments. This study demonstrates *in situ* TEM implementation and fabrication of three-terminal devices with nanometer features from a 2D material and, importantly, their *in situ* operation. Extending this work, we envision a wide range of *in situ* TEM transport experiments in nanoscale systems that exploit the TEM's atomic precision to study and understand correlations between transport phenomena and atomic structure.

RESULTS AND DISCUSSION

Observations were carried out with an electron microscope (JEOL 2010F) operated at 200 kV. TEM-compatible chips were mounted in a sample holder with electrical feedthroughs (Hummingbird Scientific) for electronic-transport measurements. Chips were fabricated with standard photolithography, electron-beam lithography, and etching processes (a detailed description is given in the Methods section). Briefly, we used 100-nm-thick SiN_x films spanning areas of $\sim 60 \times 60$ μm^2 as insulating supports for metal electrodes and graphene and as electron-transparent windows. In each chip, graphene was patterned into a 2- μm -wide strip in contact with the three electrodes. Freestanding-graphene areas were obtained by making gaps in the SiN_x film with a focused ion beam prior to graphene deposition (Figure 2a). Electron diffraction and electron energy-loss spectroscopy confirmed the presence of graphene between the electrodes (see Supporting Information SI-1).

We made the GNR and graphene gate electrode of each device with the same *in situ* fabrication process by appropriately cutting the continuous freestanding graphene strip with the electron beam. The beam was focused into a probe and scanned over the sample in STEM mode following a preprogrammed series of parallel and perpendicular lines designed to achieve the desired geometry: a single GNR with an isolated graphene side gate nearby. The beam energy onset for displacement of carbon atoms from graphene is ~ 90 keV.²⁴ Hence, set at 200 keV, the beam used in our experiments can cut through graphene. For this energy the knock-on displacement cross section for a carbon atom in graphene is ~ 15 barn.^{24,25} Therefore, to displace all carbon atoms from an area of 1 nm² requires $\sim 10^9$ electrons (1 nm²/15 barn). This corresponds to an irradiation dose (charge per unit area) of 10^8 C m⁻². A lower dose would cause less damage to the lattice. High-angle annular dark-field (HAADF) STEM images are composed with the signal from electrons scattered with angles

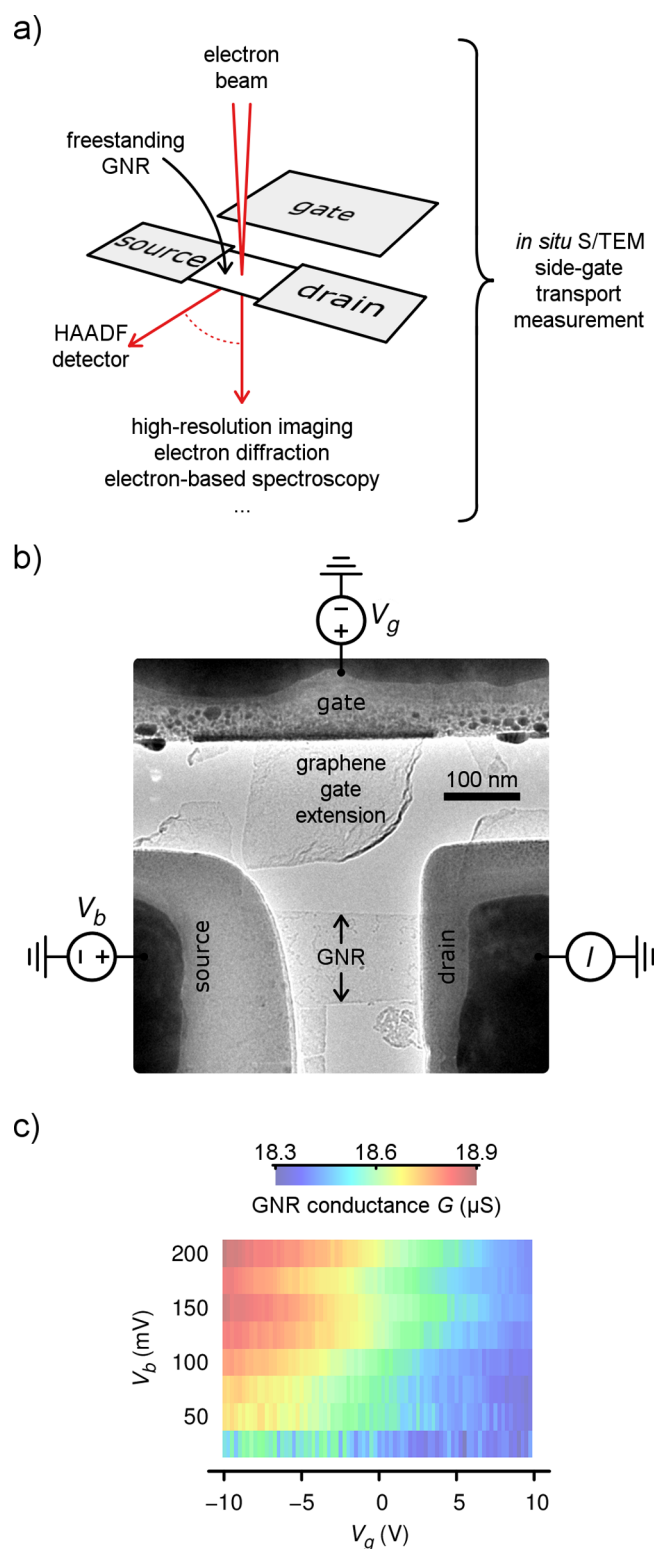


Figure 1. *In situ* TEM side-gate transport measurement in a freestanding graphene nanoribbon (GNR) fabricated *in situ* in the TEM. (a) Scheme of three-electrode chip configuration used to perform *in situ* TEM transport measurements of a GNR. The electron beam is shown focused, as in the STEM mode. (b) TEM image of typical GNR obtained after sculpting a graphene sheet with the electron beam. Source, drain, and side-gate metal electrodes are visible on top of the SiN_x film. The distance between the gate extension carved from graphene and the GNR is ~ 80 nm. Two voltage sources (V_b and V_g) and an ammeter

Figure 1. continued

compose the electrical circuit. (c) Color plot of GNR conductance showing transport modulation as a function of source–drain and side-gate voltages V_b and V_g for a GNR with a width and length of 68 ± 2 and 187 ± 3 nm, respectively. The distance between the GNR and gate extension was 80 ± 5 nm. The measurement was performed at room temperature within the TEM.

> 50 mrad with each pixel's intensity proportional to the mass probed by the beam. This mass contrast readily distinguishes the presence and absence of graphene in HAADF STEM images. Bearing in mind the above considerations, the procedure to sculpt graphene comprises the following steps:^{22,23} (1) acquiring a HAADF STEM reference image with a low irradiation dose ($\sim 10^3$ C m⁻²) to minimize damage in the graphene area to be modified, (2) designing a cutting path using the acquired reference image, and (3) driving the beam through the designed path with a dosage high enough to cut graphene ($\sim 10^8$ C m⁻²). The beam can be placed at any point within the reference HAADF STEM image. Thus, any pattern can be engraved in graphene, as illustrated in Figure 2b

with the cutting of a line. We used a 2-nm-diameter probe with a current of 3 nA (current density $\sim 10^9$ A m⁻²). HAADF STEM reference images were acquired with irradiation dwell times per pixel on the order of 1 μ s, with 256×256 pixels and a pixel size of <10 nm. Similar imaging conditions induced only minimal changes in the conductance of GNRs supported by SiNx films.¹⁶ To cut graphene, the dwell time per pixel was increased 5 orders of magnitude to 0.1–0.5 s.

To maximize the capacitive coupling between GNR and gate electrode, the separation between them was kept minimal to around 50–150 nm by sculpting a gate extension from the graphene strip (Figure 2c), connected to a larger Au electrode. As explained below, according to numerical calculations the electric field at the GNR channel is expected to be ~ 3 times stronger with than without the graphene gate extension (*i.e.*, only the Au electrode). We also used the electron-beam-based sculpting procedure to reduce the GNR's width in each device by gradually reducing the width of the original GNR (Figure 2d).

Graphene was annealed *via* Joule heating before, during, and after sculpting with currents up to 10^{-4} A, yielding current densities on the order of 10^{12} A m⁻² (see Supporting

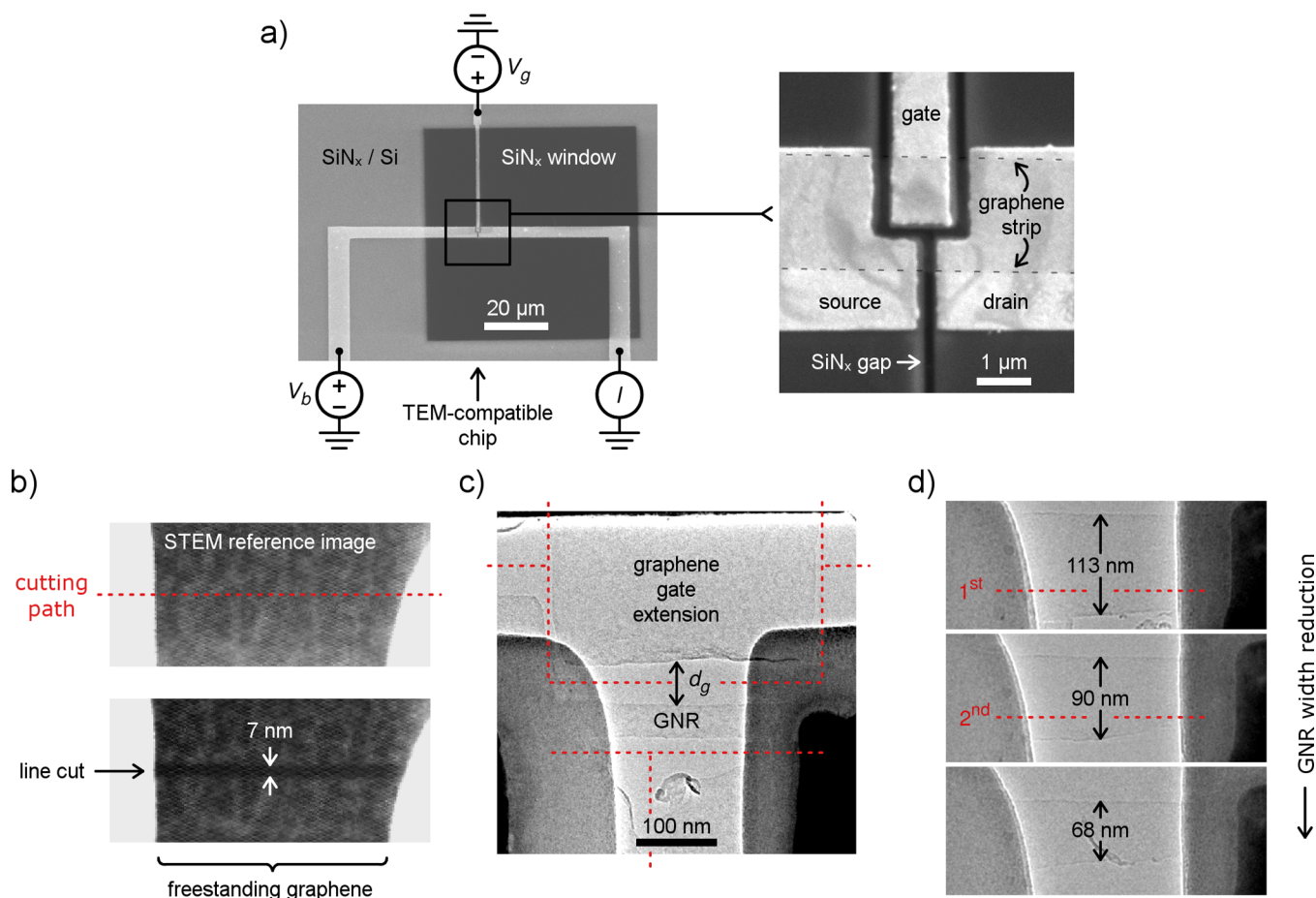


Figure 2. Fabrication of freestanding GNRs in TEM-compatible chips. (a) SEM image of a three-electrode chip in an electron-transparent SiNx window. The magnified area (right) shows the initial graphene strip in contact with all electrodes; dashed lines mark the graphene strip borders. (b) Cutting of a line in freestanding graphene. The top HAADF STEM image served as reference for the cutting path indicated by the dotted line. The bottom image shows the same area with a 7-nm-wide line cut, after the electron beam was rastered through the path. The SiNx-gap ends are visible as gray areas. (c) TEM image of a GNR in proximity to the graphene gate extension. The double-headed arrow indicates the distance d_g between the GNR and extension. Dotted lines illustrate cutting paths used for sculpting the graphene strip. (d) TEM images showing GNR width reduction (from top to bottom). Dotted lines indicate the first and second cutting paths used to reduce the width of the same GNR. The images' brightness and contrast were modified for clarity.

Information SI-2). With these conditions graphene can be heated to temperatures above 1000 K.²⁶ Annealing avoids contamination by enhancing diffusion of mobile hydrocarbons, increases the rate of recombination of defects (interstitials and vacancies), and induces crystallization of amorphous carbon.^{18,26–28} The described annealing effects help to contain electron-irradiation-induced damage in the GNRs.

To model the effect of the side gate on the GNR conductance in our *in situ* TEM transport measurements, we estimated numerically the electrostatic potential V at the channel for the electrode geometry in our experiment (Figure 3a). In this analysis, the central point of the channel closest to the gate electrode is defined as p_0 , and the distance between channel and gate is defined as d_g . From each electric potential distribution V , we derived the electric field strength E (see Supporting Information SI-3 for details). The effect of extending the gate spatially, from the Au electrode toward the channel, on the electric field E is shown in Figure 3b, where we plot E at p_0 for different d_g as a function of V_g . It is at this point in the area covered by a GNR that the E is strongest. Hence, with our chip configuration we expect maximum values of $E \approx 10^7$ V m⁻¹ at p_0 . To put this value in perspective, we compare it to the E in a back-gate FET device with a 300 nm thick SiO₂ gate layer, an arrangement commonly used for GNR devices. For a 1 V gate potential the electric field strength is about the same, $E \approx 0.3 \times 10^7$ V m⁻¹ at p_0 , in both the back- and side-gate configurations, when $d_g = 100$ nm in the latter case. However, the charging effect will be approximately 4 times stronger in the back-gate configuration because the permittivity of SiO₂ is $3.9 \times$ permittivity of vacuum (the pressure in the TEM column is 10^{-5} Pa). In addition, the E magnitude decays as the distance in the channel from the side-gate electrode increases (Figure 3c).

We present results from three nanosculpted devices tested at room temperature, the TEM's column operating temperature. During all transport measurements the electron beam was blocked to avoid the electron-beam-induced damage of the GNRs. The V_g sweep was restricted to a ± 10 V range to prevent leakage currents through the SiN_x film and the devices' mechanical collapse due to electrostatic forces.²⁹ Details of the measurements and leakage current analysis are provided in Supporting Information SI-4. Figure 4a and b show the conductance G and $\Delta G = G - G_0$, respectively, where G_0 is G evaluated at $V_g = 0$, as a function of V_g for three GNRs with widths W of 113 ± 2 , 68 ± 2 , and 31 ± 3 nm. The GNR length L in each device is defined by the SiN_x gap's length. Since the GNR that was 68 nm wide was obtained by cutting the GNR that was initially 113 nm wide (see Figure 2d), these two same-chip devices had the same L (187 ± 3 nm) and d_g (80 ± 5 nm). The GNR with a width of 31 nm wide was patterned in another chip with $L = 182 \pm 2$ nm and $d_g = 58 \pm 4$ nm. The quoted distances for W and d_g correspond to values averaged along each GNR length. For these measurements the source–drain voltage was set to $V_b = 0.1$ V.

In addition to demonstrating the modulation of a GNR channel's conductance with a side-gate electrode within a TEM column, these results indicate that the side-gate electrode's capacity to modulate the conductance increases as the GNR width decreases. In particular, changes in G were only registered as the GNR width in each device was reduced from an initial value of $W \approx 1$ μ m to a few tens of nanometers. The trend is evident when comparing the GNRs' ΔG values (Figure 4b). The GNR that was 113 nm wide shows $\Delta G \approx 0$

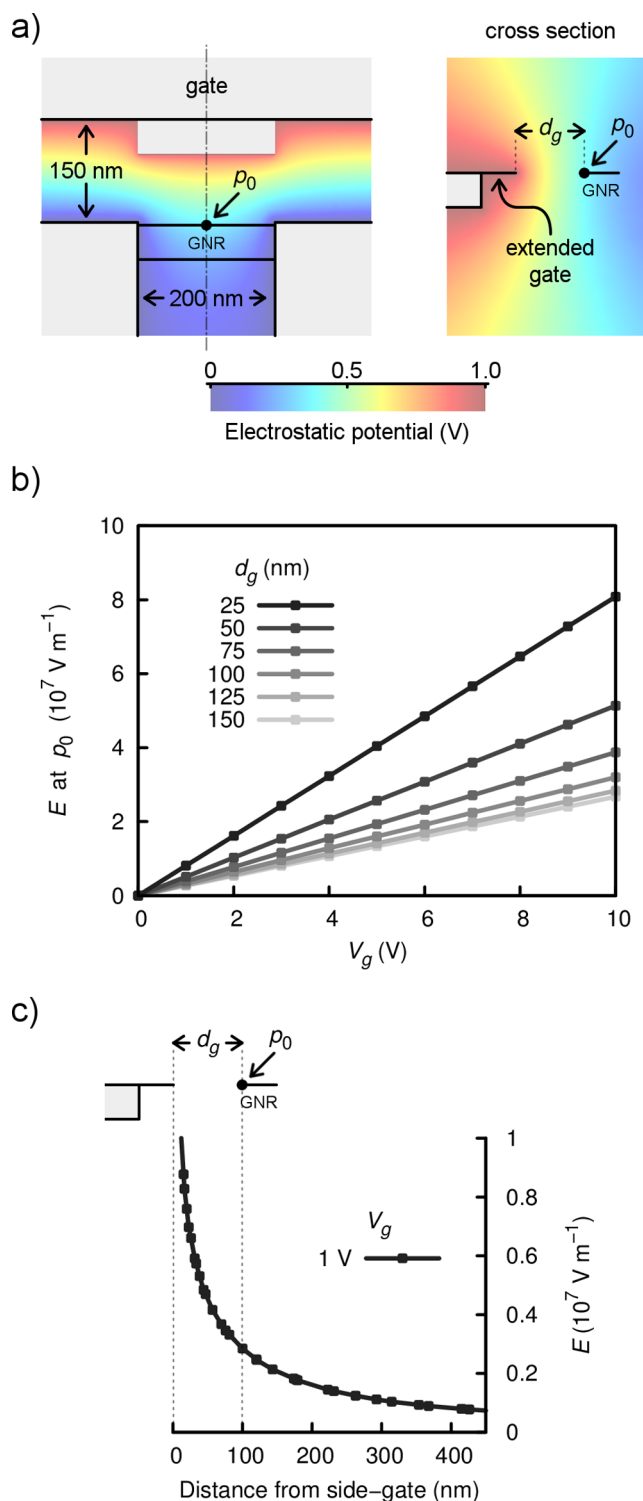


Figure 3. Numerical calculations of electrostatic potential and electric field induced by side-gate electrode. (a) Electrostatic potential for side-gate voltage $V_g = 1$ V and source and drain electrodes grounded ($V = 0$ V). In this example, the distance from the extended gate to the channel $d_g = 100$ nm. The dash-dotted line indicates the plane from which the cross section (right) was taken. The potential at p_0 , the closest point from gate to channel in this model, is not zero. (b) Electric field strength E at p_0 as a function of V_g for six different distances d_g . When $d_g = 150$ nm the extension of the gate, carved from graphene in the experiment, is zero in this model. (c) Electric field strength E as a function of distance from

Figure 3. continued

the side gate in a line passing through p_0 . Here, we use the same geometrical parameters as in (a).

for all V_g in contrast to the other two narrower GNRs for which $\Delta G \neq 0$ in the same V_g range. In general, as the W/L channel ratio of a FET device increases, short-channel effects result in a weakened gate capacity to control transport.³⁰ This effect has been observed in back-gated GNR devices³¹ but should be more pronounced in our devices because the electric field strength decreases along the GNR width (see Figure 3c). In addition, GNRs have energy gaps $\sim 1/W$ that lead to larger $I_{\text{on}}/I_{\text{off}}$ ratios for narrower GNRs.^{32,33} These effects coincide qualitatively with our result that the side-gate's capacity to modulate transport is stronger for narrower GNRs.

The GNR conductance of the analyzed GNRs ($G \approx 17, 19$, and $22 \mu\text{S}$ for GNR width $W = 31 \pm 3, 68 \pm 2$, and 113 ± 2 nm, respectively) is close to the expected minimum conductance of $\sim (e^2/h) \times (W/L)$ for a GNR at room temperature,³² suggesting that the as-fabricated GNRs are not in the on-state. However, the gate-voltage range ($|V_g| \leq 10$ V) prevented us from establishing the full on/off-state response of the studied GNR devices. Considering the sense of the registered changes in G as a function of V_g ($\Delta G/\Delta V_g < 0$), our measurements are consistent with that of p-type GNRs that are in an electronic state close to the minimum conductance with a charge-neutrality point at $V_g > 0$. The shift of the charge-neutrality point is most likely caused by impurities and substrate effects in graphene areas adjacent to the freestanding channel. For the narrowest GNR device ($W = 31 \pm 3$ nm) we estimated a subthreshold swing $S \approx \Delta V_g/\Delta(\log I)$,³⁰ which quantifies the efficiency to turn on and off a FET-type device, of $S \approx 860 \text{ V dec}^{-1}$. By comparison, a back-gated (300-nm-thick SiO_2 gate layer) GNR that is 24 nm wide (from exfoliated graphene) was shown to have an $S \approx 80 \text{ V dec}^{-1}$ at room temperature.³² Assuming similar graphene conductivity in both cases, the side-gate device is 10 times less efficient, in agreement with a lower channel-gate capacitive coupling in the side-gate configuration, recalling that for this configuration we estimate a 4-fold weaker charging effect (at p_0) from the calculated electric field. Possible improvements to boost the coupling between side-gate and channel include reducing the distance d_g , adding dielectric layers to partially fill the vacuum gap between gate and channel, and patterning an additional side-gate electrode opposite the first to reduce the asymmetry of the electric field at the channel and increase its strength. In the end, changes in chip configuration will have to be tailored according to a channel's material and size.

The combination of GNR width reduction and annealing produced channels a few nanometers wide that ultimately failed by channel rupture. The graphene-derived structures obtained before failure resembled constrictions^{13–15} rather than well-defined ribbons but also displayed modulation in G as a function of V_g . An example of a constriction and its conductance response is shown in Figure 4c. This constriction was formed in the middle of a GNR ($W = 50 \pm 2$ nm and $L = 180 \pm 3$ nm) and consisted of two separated channels with an average length of roughly 10 nm. One channel resembles a 12-nm-wide GNR and the other, with $a < 2$ nm span at its narrowest point, a carbon nanotube. For this constriction G showed a peak (about $V_g = -5$ V) similar to those observed in devices possessing negative differential conductance. At this

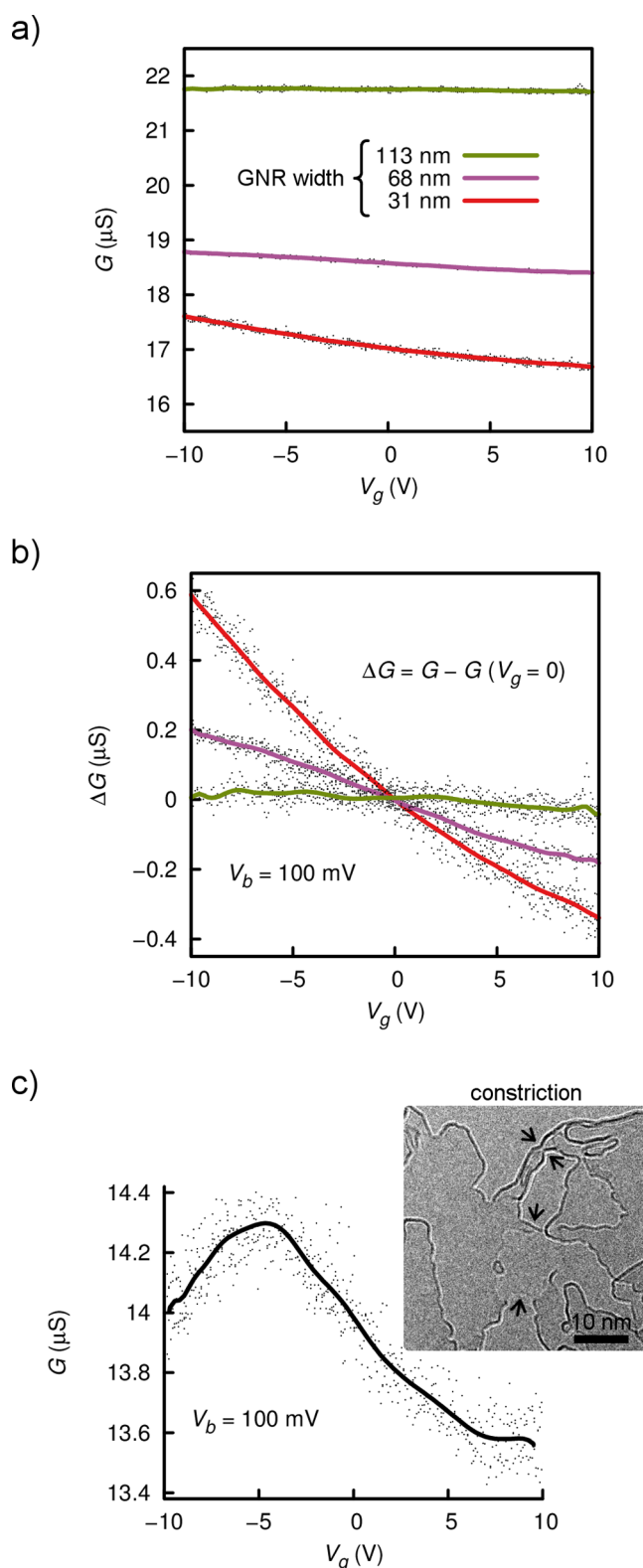


Figure 4. Side-gate modulation of GNR conductance within the TEM column. (a) GNR conductance G and (b) $\Delta G = G - G_0$, where G_0 is G evaluated at $V_g = 0$, as a function of V_g in three GNRs with widths of $113 \pm 2, 68 \pm 2$, and 31 ± 3 nm. Values of $\Delta G \neq 0$ indicate that the GNR conductance was modulated by the side-gate potential. (c) Conductance as a function of V_g in a graphene-derived constriction. Inset: TEM image of channel composed of two paths (indicated by arrows) separated by a hole in the structure. The paths are 12 and <2 nm wide at their narrowest

Figure 4. continued

points. During these measurements the source–drain voltage was set to $V_b = 0.1$ V. All lines are a noise-reduction fit to each raw data set (black points).

point we can only speculate the origin of this peak, but given the relative short length of the constriction, a resonant tunneling effect cannot be discarded, and more studies would be needed to fully understand this observation. For example, by increasing the image resolution with an aberration-corrected TEM, this observation could be correlated with the precise atomic arrangement and edge structure (armchair, zigzag, roughness, etc.) of the GNR.

CONCLUSIONS

In summary, we carried out *in situ* TEM transport measurements with devices fabricated *in situ* that contain a side-gate electrode that modulates the carrier density in a freestanding channel a few nanometers wide. In particular, we outline the STEM procedure to form gated graphene structures, and we demonstrate the resulting side-gate-induced modulation of conductance at room temperature in GNRs fabricated within the TEM column. This emphasizes that our approach enables both a full characterization of the active channel in an FET-type configuration and structural modifications of the device *via* electron-beam sculpting. With state-of-the-art instrumentation the spatial resolution of both the channel characterization (structural and chemical) and beam-induced modifications can be pushed to the atomic level. The combined method of beam-induced channel modifications with *in situ* TEM transport measurements is especially well-suited for other 2D materials, provided that the specific beam energy and dose requirements have been met. With slight modifications this method can be applied to investigate transport phenomena in nanoscale systems, such as single-molecule transport or metal-to-insulator transitions dependent on channel width or edge structure, where the resolution of the channel's atomic structure is of paramount importance.

METHODS

Graphene Growth. We used graphene grown *via* atmospheric pressure chemical vapor deposition on Cu foil (99.8% purity).³⁴ For graphene growth the Cu foil is sonicated in acetone for 10 min and then dried with N_2 after rinsing in deionized water. Then, the foil is inserted into a sealed 1 in. quartz tube furnace. A mixture of Ar (500 sccm) and H_2 (50 sccm) is introduced into the tube for 10 min to flush the tube. Afterwards, the furnace is set to 1057 °C, the H_2 flow is reduced to 25 sccm, and 2 sccm of a 1% CH_4 in an Ar mixture is flowed into the tube. After 100 min of growth the furnace is turned off and the tube is moved to a position where the foil is 2 in. away from the furnace entrance. Once the oven reaches 850 °C, the flow rates for Ar, H_2 , and CH_4 are changed to 1000, 7, and 0 sccm, respectively. Finally, the foil is removed when the tube reaches room temperature.

Fabrication Details of TEM-Compatible Chips. Si/SiN_x substrates (from WRS Materials) consisting of 300-nm-thick Si wafers covered by 100-nm-thick low stress (<100 MPa) SiN_x films were patterned and etched to fabricate 5×3.5 mm² chips, with each chip containing an area $\sim 60 \times 60$ μm^2 of freestanding SiN_x film resembling a “window”. The SiN_x window is transparent to the electron beam and supports the device's metal electrodes and graphene. The windows were fabricated by, first, etching the SiN_x with SF₆ from squares (450×450 μm^2) patterned with photolithography in one side of the wafer and, second, etching the exposed Si with a KOH bath. T-shaped Au/Cr electrodes with thicknesses of 50–100/10 nm were fabricated in

the windows with photolithography followed by metal thermal evaporation. To allow for freestanding graphene areas, a fork-shaped gap 150–200 nm wide was made in the windows containing electrodes with a focused ion beam with Ga source. Then, the windows were completely covered by CVD-grown graphene. After transferring a continuous film of graphene into the SiN_x window a protective strip 2 μm wide of poly(methyl methacrylate) (PMMA) covering the graphene was patterned at the intersection of the electrodes with electron-beam lithography. The graphene outside the protective strip was etched with O₂ plasma and, finally, the PMMA resist was removed. For *in situ* TEM transport measurements, the TEM-compatible devices were pasted and wire-bonded to TEM chip carriers, which in turn were mounted to a sample holder with electrical feedthroughs (Hummingbird Scientific).

ASSOCIATED CONTENT

Supporting Information

The Supporting Information is available free of charge on the ACS Publications website at DOI: 10.1021/acs.nano.6b01419.

Details for graphene characterization and annealing *via* Joule heating; calculation of the electrostatic potential and electric field; and transport measurements and leakage current analysis (PDF)

AUTHOR INFORMATION

Corresponding Authors

*E-mail (A. T. C. Johnson): cjohnson@physics.upenn.edu.

*E-mail (M. Drndić): drndic@physics.upenn.edu.

Present Address

[§]Department of Electronic Engineering, Kwangwoon University, Seoul 01897, South Korea.

Author Contributions

[‡]J. A. Rodríguez-Manzo and Z. J. Qi contributed equally to this work.

Author Contributions

J.A.R.-M., Z.J.Q., A.T.C.J., and M.D. designed the experiments; J.A.R.-M., Z.J.Q., and A.C. prepared the samples. J.A.R.-M. and Z.J.Q. performed *in situ* TEM transport measurements. All authors contributed to data analysis and the manuscript writing.

Notes

The authors declare no competing financial interest.

ACKNOWLEDGMENTS

We acknowledge support from NIH Grants R21004767 and R21HG007856 and access to the TEM NSF-MRSEC facility at the University of Pennsylvania. Z.J.Q. and A.T.C.J. acknowledge support from SRC Contract No. 2011-IN-2229, associated with NSF AIR Program ENG-1312202. Z. J. Q. acknowledges support from the IBM Ph.D. Fellowship and the NSF IGERT program (Grant DGE02-21664). The authors thank Andrés R. Botello-Méndez and Prof. Vincent Meunier for fruitful discussions.

REFERENCES

- (1) Ohnishi, H.; Kondo, Y.; Takayanagi, K. Quantized Conductance Through Individual Rows of Suspended Gold Atoms. *Nature* **1998**, *395*, 780–783.
- (2) Erts, D.; Olin, H.; Ryen, L.; Olsson, E.; Thölén, A. Maxwell and Sharvin conductance in gold point contacts investigated using TEM-STM. *Phys. Rev. B: Condens. Matter Mater. Phys.* **2000**, *61*, 12725–12727.

- (3) Kizuka, T.; Umehara, S.; Fujisawa, S. Metal-Insulator Transition in Stable One-Dimensional Arrangements of Single Gold Atoms. *Jpn. J. Appl. Phys.* **2001**, *40*, L71.
- (4) Wang, Z. L.; Poncharal, P.; de Heer, W. A. Measuring Physical and Mechanical Properties of Individual Carbon Nanotubes by *In Situ* TEM. *J. Phys. Chem. Solids* **2000**, *61*, 1025–1030.
- (5) Huang, J. Y.; Chen, S.; Jo, S. H.; Wang, Z.; Han, D. X.; Chen, G.; Dresselhaus, M. S.; Ren, Z. F. Atomic-Scale Imaging of Wall-by-Wall Breakdown and Concurrent Transport Measurements in Multiwall Carbon Nanotubes. *Phys. Rev. Lett.* **2005**, *94*, 236802.
- (6) Wang, M. S.; Wang, J. Y.; Chen, Q.; Peng, L. M. Fabrication and Electrical and Mechanical Properties of Carbon Nanotube Interconnections. *Adv. Funct. Mater.* **2005**, *15*, 1825–1831.
- (7) Cumings, J.; Zettl, A. Field Emission and Current-Voltage Properties of Boron Nitride Nanotubes. *Solid State Commun.* **2004**, *129*, 661–664.
- (8) Golberg, D.; Mitome, M.; Kurashima, K.; Zhi, C. Y.; Tang, C. C.; Bando, Y.; Lourie, O. *In situ* electrical probing and bias-mediated manipulation of dielectric nanotubes in a high-resolution transmission electron microscope. *Appl. Phys. Lett.* **2006**, *88*, 123101.
- (9) Kizuka, T.; Takatani, Y.; Asaka, K.; Yoshizaki, R. Measurements of the Atomistic Mechanics of Single Crystalline Silicon Wires of Nanometer Width. *Phys. Rev. B: Condens. Matter Mater. Phys.* **2005**, *72*, 035333.
- (10) Nam, S.-W.; Chung, H.-S.; Chieh Lo, Y.; Qi, L.; Li, J.; Lu, Y.; Johnson, A. T. C.; Jung, Y.; Agarwal, R. Electrical Wind Force-Driven and Dislocation-Templated Amorphization in Phase-Change Nanowires. *Science* **2012**, *336*, 1561–1566.
- (11) Lin, J.; Cretu, O.; Zhou, W.; Suenaga, K.; Prasai, D.; Bolotin, K. I.; Cuong, N. T.; Otani, M.; Okada, S.; Lupini, A. R.; Idrobo, J.-C.; Caudel, D.; Burger, A.; Chimire, N. J.; Yan, J.; Mandrus, D. G.; Pennycook, S. J.; Pantelides, S. T. Flexible Metallic Nanowires with Self-Adaptive Contacts to Semiconducting Transition-Metal Dichalcogenide Monolayers. *Nat. Nanotechnol.* **2014**, *9*, 436–442.
- (12) Rodríguez-Manzo, J. A.; Banhart, F.; Terrones, M.; Terrones, H.; Grobert, N.; Ajayan, P. M.; Sumpter, B. G.; Meunier, V.; Wang, M.; Bando, Y.; Golberg, D. Heterojunctions between Metals and Carbon Nanotubes as Ultimate Nanocontacts. *Proc. Natl. Acad. Sci. U. S. A.* **2009**, *106*, 4591–5.
- (13) Lu, Y.; Merchant, C. A.; Drndić, M.; Johnson, A. T. C. *In Situ* Electronic Characterization of Graphene Nanoconstrictions Fabricated in a Transmission Electron Microscope. *Nano Lett.* **2011**, *11*, 5184–5188.
- (14) Barreiro, A.; Börrnert, F.; Rummeli, M. H.; Büchner, B.; Vandersypen, L. M. K. Graphene at High Bias: Cracking, Layer by Layer Sublimation, and Fusing. *Nano Lett.* **2012**, *12*, 1873–1878.
- (15) Börrnert, F.; Barreiro, A.; Wolf, D.; Katsnelson, M. I.; Büchner, B.; Vandersypen, L. M. K.; Rummeli, M. H. Lattice Expansion in Seamless Bilayer Graphene Constrictions at High Bias. *Nano Lett.* **2012**, *12*, 4455–4459.
- (16) Puster, M.; Rodríguez-Manzo, J. A.; Balan, A.; Drndić, M. Toward Sensitive Graphene Nanoribbon–Nanopore Devices by Preventing Electron Beam-Induced Damage. *ACS Nano* **2013**, *7*, 11283–11289.
- (17) Qi, Z. J.; Rodríguez-Manzo, J. A.; Botello-Méndez, A. R.; Hong, S. J.; Stach, E. A.; Park, Y. W.; Charlier, J.-C.; Drndić, M.; Johnson, A. T. C. Correlating Atomic Structure and Transport in Suspended Graphene Nanoribbons. *Nano Lett.* **2014**, *14*, 4238–4244.
- (18) Qi, Z. J.; Daniels, C.; Hong, S. J.; Park, Y. W.; Meunier, V.; Drndić, M.; Johnson, A. T. C. Electronic Transport of Recrystallized Freestanding Graphene Nanoribbons. *ACS Nano* **2015**, *9*, 3510–3520.
- (19) Cretu, O.; Botello-Mendez, A. R.; Janowska, I.; Pham-Huu, C.; Charlier, J.-C.; Banhart, F. Electrical Transport Measured in Atomic Carbon Chains. *Nano Lett.* **2013**, *13*, 3487–3493.
- (20) Yamamoto, K.; Iriyama, Y.; Asaka, T.; Hirayama, T.; Fujita, H.; Fisher, C. A. J.; Nonaka, K.; Sugita, Y.; Ogumi, Z. Dynamic Visualization of the Electric Potential in an All-Solid-State Rechargeable Lithium Battery. *Angew. Chem., Int. Ed.* **2010**, *49*, 4414–4417.
- (21) Huang, J. Y.; Zhong, L.; Wang, C. M.; Sullivan, J. P.; Xu, W.; Zhang, L. Q.; Mao, S. X.; Hudak, N. S.; Liu, X. H.; Subramanian, A.; Fan, H.; Qi, L.; Kushima, A.; Li, J. *In Situ* Observation of the Electrochemical Lithiation of a Single SnO₂ Nanowire Electrode. *Science* **2010**, *330*, 1515–1520.
- (22) Börrnert, F.; Fu, L.; Gorantla, S.; Knupfer, M.; Büchner, B.; Rummeli, M. H. Programmable Sub-nanometer Sculpting of Graphene with Electron Beams. *ACS Nano* **2012**, *6*, 10327–10334.
- (23) Xu, Q.; Wu, M.-Y.; Schneider, G. F.; Houben, L.; Malladi, S. K.; Dekker, C.; Yucelen, E.; Dunin-Borkowski, R. E.; Zandbergen, H. W. Controllable Atomic Scale Patterning of Freestanding Monolayer Graphene at Elevated Temperature. *ACS Nano* **2013**, *7*, 1566–1572.
- (24) Meyer, J. C.; Eder, F.; Kurasch, S.; Skakalova, V.; Kotakoski, J.; Park, H. J.; Roth, S.; Chuvilin, A.; Eyhusen, S.; Benner, G.; Krashennnikov, A. V.; Kaiser, U. Accurate Measurement of Electron Beam Induced Displacement Cross Sections for Single-Layer Graphene. *Phys. Rev. Lett.* **2012**, *108*, 196102.
- (25) Egerton, R. F.; Li, P.; Malac, M. Radiation Damage in the TEM and SEM. *Micron* **2004**, *35*, 399–409.
- (26) Westenfelder, B.; Meyer, J. C.; Biskupek, J.; Kurasch, S.; Scholz, F.; Krill, C. E.; Kaiser, U. Transformations of Carbon Adsorbates on Graphene Substrates under Extreme Heat. *Nano Lett.* **2011**, *11*, 5123–5127.
- (27) Florian, B. Irradiation Effects in Carbon Nanostructures. *Rep. Prog. Phys.* **1999**, *62*, 1181.
- (28) Moser, J.; Barreiro, A.; Bachtold, A. Current-Induced Cleaning of Graphene. *Appl. Phys. Lett.* **2007**, *91*, 163513.
- (29) Bolotin, K. I.; Sikes, K. J.; Jiang, Z.; Klima, M.; Fudenberg, G.; Hone, J.; Kim, P.; Stormer, H. L. Ultrahigh Electron Mobility in Suspended Graphene. *Solid State Commun.* **2008**, *146*, 351–355.
- (30) Schwierz, F. Graphene Transistors. *Nat. Nanotechnol.* **2010**, *5*, 487–496.
- (31) Shu-Jen, H.; Zhihong, C.; Bol, A. A.; Sun, Y. Channel-Length-Dependent Transport Behaviors of Graphene Field-Effect Transistors. *IEEE Electron Device Lett.* **2011**, *32*, 812–814.
- (32) Han, M. Y.; Özyilmaz, B.; Zhang, Y.; Kim, P. Energy Band-Gap Engineering of Graphene Nanoribbons. *Phys. Rev. Lett.* **2007**, *98*, 206805.
- (33) Li, X.; Wang, X.; Zhang, L.; Lee, S.; Dai, H. Chemically Derived, Ultrasoft Graphene Nanoribbon Semiconductors. *Science* **2008**, *319*, 1229–1232.
- (34) Luo, Z.; Lu, Y.; Singer, D. W.; Berck, M. E.; Somers, L. A.; Goldsmith, B. R.; Johnson, A. T. C. Effect of Substrate Roughness and Feedstock Concentration on Growth of Wafer-Scale Graphene at Atmospheric Pressure. *Chem. Mater.* **2011**, *23*, 1441–1447.